

Ice Fabric Inference with Thin-Section Measurements and Sonic Velocities with Application to the NEEM Ice Core

Michael J. Hay¹, Erin C. Pettit², and Edwin D. Waddington¹ and M. Montagnat¹

¹*Department of Earth and Space Sciences, University of Washington, Seattle, WA, USA*

²*Geophysical Institute, University of Alaska, Fairbanks, AK, USA*

³*IGE, Universit Grenoble Alpes/CNRS, Grenoble, France*

ABSTRACT. We explore methods of inferring crystal orientation fabric using sound waves in ice-core boreholes, in tandem with velocity data from ice-core thin sections. We pay particular attention to sonic-velocity data collected from the NEEM ice core. Thin-section fabric measurements have been the predominant way of inferring crystal fabric from boreholes. However, thin-section measurements suffer from sampling error, and do not provide a spatially continuous record of fabric. Sonic velocity measurements in boreholes allow for spatially-continuous measurements of fabric, and largely eliminate sampling error. Unfortunately, fabric inference from sonic velocity measurements suffer from error from inferring fabric from sonic velocities due to using an imperfect sonic-velocity model (model error). In addition, the sonic tool used at NEEM suffered from error due to poor tool centering in the borehole. It also only collected P-wave velocities, which are only sensitive to the largest fabric eigenvalue. To address these difficulties, we introduce a method of combining sonic velocity measurements with fabric measurements. We show that this new method suffers from significantly less sampling error than thin-section measurements alone do, while greatly reducing model error and the effects of poor tool centering. We apply this method to fabric thin-section data and sonic-velocity data collected at NEEM to produce a spatially-continuous and accurate record of fabric.

1. INTRODUCTION

Ice is a highly viscoplastically anisotropic material, deforming most easily in shear parallel to the basal plane, orthogonal to the crystallographic c-axis. The distribution of c-axis orientations in a polycrystal is known as the orientation distribution function (ODF). The bulk strain rate of a polycrystal can vary by an order of magnitude, depending on the ODF (Thorsteinsson and Waddington, 2002). The ODF is an antipodally-symmetric probability distribution on the sphere, giving the density of c-axes by orientation across the sphere. Commonly, ODFs are summarized by the second-order orientation tensor, which is the second moment \mathbf{A} of the ODF. That is, the average of the outer product of the c-axis with itself, $\mathbf{c} \otimes \mathbf{c}$, taken over the ODF. Equivalently, the second-order orientation tensor is the covariance matrix of c-axis directions. An estimate $\tilde{\mathbf{A}}$ of the second-order orientation tensor can be found from a thin-section sample as,

$$\tilde{\mathbf{A}} = \sum_i \zeta_i \mathbf{c}_i \otimes \mathbf{c}_i, \quad (1)$$

where there are N grains \mathbf{c}_i in the sample, with $i = 1, \dots, N$. Also, ζ_i is the area of grain i , where the areas are normalized such that the total area of the thin section is unity.

The eigenvalues λ_i of this tensor provide a measure of fabric concentration in each of the three corresponding eigenvectors, or fabric principal-directions. The largest eigenvalue, λ_3 , is associated with the direction of the greatest c-axis concentration. The smallest, λ_1 , is associated with the direction of least concentration. The middle eigenvalue, λ_2 , is associated with the direction orthogonal to the other two. The eigenvalues sum to unity by construction. If $\lambda_3 \approx \lambda_2 \approx \lambda_1$, the fabric is isotropic. If $\lambda_3 \gg \lambda_2 \approx \lambda_1$, the ODF exhibits a single-maximum fabric, with a large concentration in one direction. If $\lambda_3 \approx \lambda_2 \gg \lambda_1$, then the concentration lies along a great circle orthogonal to the direction associated with λ_1 . This is known as a girdle fabric.

If c-axis directions of a polycrystal are distributed uniformly across the sphere, the polycrystal has bulk isotropic viscosity. However, ice undergoing deformation develops a non-uniform ODF. C-axes tend to rotate towards the directions of principal compression due to lattice rotation during deformation (Alley, 1988). This induces bulk anisotropic flow.

In ice sheets, ice crystals are usually somewhat randomly oriented at deposition, although preferred orientations have been observed in the firn column close to the surface (Placidi and others 2010, Durand and others 2009). Vertical compression causes c-axes to rotate towards the vertical direction. Likewise, shear on horizontal planes develops vertical-maximum fabrics due to the combined pure shear and rotation. Near divides, horizontal extension in one direction, and compression along the other two axes often causes vertical girdle fabrics to develop (Alley, 1988).

In addition to strongly affecting ice flow, the ODF seems to be sensitive to climate at the time of deposition. Initial perturbations in fabric due to climate can persist into deep layers (Kennedy and others, 2013). In thin sections from the NEEM core (Montagnat and others, 2014), there is an abrupt change in fabric corresponding to the Holocene boundary.

Orientation distribution functions are commonly estimated from ice thin sections taken from ice cores, typically consisting of several hundred grains. This provides a direct sample of the ODF from the section of ice, but suffers from sampling error. This sampling error can be especially severe due to the typically highly non-uniform distribution of grain sizes. Polycrystal properties are best weighted by area in the thin section (Gagliardini and others, 2004); if several large grains cover much of the thin-section area, the effective sample size can be much smaller than the number of sampled grains.

In addition to sampling error, thin-section samples have very limited spatial coverage, usually on the order of 100 cm^2 . Thin-section samples are labor intensive and consume core ice. Due to this, thin-section samples are typically taken only on the order of every tens of meters. Therefore, thin-section samples cannot capture fabric variability at shorter length scales. In addition, if one is interested in fabric characteristics averaged over several cubic meters, rather than a single thin section, short length-scale fabric variability (on the scale of decimeters) introduces another source of error.

Bentley (1972) first proposed sonic logging as a method of fabric measurement to ameliorate some of the difficulties of thin-section fabric measurements. In addition to being viscously anisotropic, ice is elastically anisotropic. Therefore, sonic velocities of individual ice crystals are dependent on grain orientation. The stiffness tensor of a polycrystal is dependent on the orientation of the constituent grains. Sonic velocity measurements holds several advantages over thin-section fabric measurements. Sonic logging tools can sample on the order of 3 m^3 of ice (Kluskiwicz and others, 2017), which nearly eliminates sampling error, and can reduce the influence of small-scale variability in fabric.

In addition to fabric, sonic velocity in ice is affected by pressure and temperature. P-wave velocity in ice changes by around $2.5 \text{ m s}^{-1} \text{ K}^{-1}$ to $2.8 \text{ m s}^{-1} \text{ K}^{-1}$, which is a significant issue in polythermal ice (e.g. Helgerud and others 2009, Vogt and others 2008). This can cause differences in velocity on the order of 100 m s^{-1} in ice sheets (Gusmeroli and others, 2012). The effects of pressure are more modest in ice sheets, with velocity changing by around $0.2 \text{ m s}^{-1} \text{ MPa}^{-1}$ (Helgerud and others, 2009).

Recently, Maurel and others (2016) developed analytical expressions for the elasticity tensors and sonic velocities of ice for several ODF types. These included single-maximum fabrics with c-axis density distributed uniformly within a given zenith angle from vertical. In addition, they found solutions for idealized thick girdle and partial girdle fabrics. These relations have since been applied by Smith and others (2017) to infer crystal fabric in the Rutford ice stream using shear-wave splitting of seismic signals.

In this paper we outline a statistical model to infer fabric from sonic velocities using the Google Tensorflow automatic differentiation library (Abadi and others, 2016). In contrast to Maurel and others (2016), we model sonic velocities numerically using a flexible discrete approximating ODF. While this discrete ODF does not admit analytical estimates of sonic velocities (as with Maurel and others 2016), it can accurately represent a much broader range of ODFs.

We apply this technique to combine pseudo P-wave and thin-section measurements taken from the NEEM ice core to find spatially continuous and more accurate fabric estimates. Unfortunately, the data collected from the NEEM core suffers from large velocity drift due to poor tool centering in the borehole. In addition, model error may be significant. To correct these errors, we incorporate thin-section measurements. While thin-section measurements lack spatial coverage, and have significant sampling error, they are unbiased (although correlated) samples of the actual crystal fabric. If the systematic velocity error (due to bias or model error) varies on length scales significantly larger than the spacing of the thin-section measurements, then the thin-section measurements can be used to estimate this error. In this way, we can combine the relative strengths of thin-section measurements (unbiasedness) and sonic-velocity measurements (spatial coverage, little sampling error), while reducing their weaknesses. We also test this technique on synthetic fabric data and sonic measurements, and show that it can effectively correct velocity drift and model error.

2. METHODS

2.1. Velocity model for sound waves in ice

We now outline the forward velocity model used to estimate sonic velocity from ice fabric. Ice crystals exhibit anisotropic stiffness, dependent on c-axis direction. Bulk stiffness of ice anisotropic polycrystals is therefore anisotropic, dependent on the orientation of individual grains.

The bulk stiffness can be estimated using a volume-weighted average of the stiffness tensor across the polycrystal,

$$\bar{C}_{ijkl} = \int_{S_2} \psi(\mathbf{c}) C_{ijkl}(\mathbf{c}), \quad (2)$$

where ψ is the ODF giving the density of c-axes at orientation \mathbf{c} , and $C_{ijkl}(\mathbf{c})$ is the stiffness tensor of an individual ice grain, with c-axis aligned to \mathbf{c} in the bulk coordinate system. Estimating bulk stiffness through volume-weighted stiffness assumes uniform strain throughout the polycrystal. The other end-member instead takes the harmonic mean of the stiffness tensor, which corresponds to a homogeneous-stress assumption. The truth is somewhere in between these two (Hill, 1952), although both produce similar predictions. We assume uniform elastic strain throughout the polycrystal, because it avoids numerical difficulties that occur with small elements of the stiffness tensor under the harmonic mean.

Sonic velocities can be derived from plane-wave solutions to the elastodynamic wave equation with zero forcing,

$$\left(\delta_{ij} \frac{d^2}{dt^2} - \rho^{-1} \bar{C}_{iklj} \frac{d^2}{dx_k dx_l} \right) u_j = 0, \quad (3)$$

where u_i is the material velocity of the polycrystal induced by the waves. Plane waves are waves of the form $u_i = f(k_j x_j - \omega t + \phi) \hat{u}_i$, where k_i is the propagation direction, \hat{u}_i is the polarization direction, ϕ is the phase shift, and ω is the phase velocity.

The function f is a scalar function of one scalar argument. It may be a sine or cosine function, for example. Substituting the expression for a plane wave into the above equation, the function f cancels out, and it can be seen that admissible plane wave solutions are those where \hat{u}_i and ω^2 are eigenvalue/eigenvector pairs of the Christoffel matrix (Aki and R., 1980), whose components are given by,

$$M_{ij} = \rho^{-1} C_{kijl} k_k k_l. \quad (4)$$

The Christoffel matrix is symmetric, because the stiffness tensor possesses symmetries such that $C_{kijl} = C_{jlik} = C_{ljk i}$. The square roots of the three eigenvalues give the pseudo P-wave velocity v_p (the fastest), and the two pseudo-shear wave velocities, v_{sh} (the slowest) and v_{sv} (intermediate speed). Unlike waves in isotropic media, the pseudo P-wave polarization is not necessarily aligned with the propagation direction, and the shear waves are not necessarily polarized orthogonal to the propagation direction. However, the polarizations are orthogonal to one another because the Christoffel matrix is symmetric. Most observed fabrics in ice sheets have a principal direction associated with the highest c-axis concentration which is approximately vertical. Therefore, the pseudo P-wave velocity is typically polarized nearly vertical.

As an alternative to stiffness averaging and solving the resulting Christoffel equations, many authors have averaged the harmonic mean of sonic velocities (or the mean of the slowness) across the ODF, instead of the stiffness tensor. While simple and intuitive, this approach ignores mode conversion between P and S waves at grain boundaries (Maurel and others, 2015).

Estimating the sonic velocities from an ODF requires computing the integral in Eq. (2). For the majority of proposed parametric ODFs, this integral must be computed numerically using quadrature on the sphere, because there do not exist analytical expressions for the integral. Again, the parametric ODFs used by Maurel and others (2016) are an exception.

Computing the integral in Eq. (2) using quadrature is done by taking a weighted sum of the value of the integrand at pre-specified quadrature points on the sphere. Our approach is to assume a discrete ODF where the support (the domain where probability density is nonzero) of the distribution is confined to the quadrature points. The distribution is parameterized by the weight of each quadrature point. While there is no density at other points on the sphere, unlike continuous ODFs, densities at non-quadrature points are irrelevant since non-quadrature points receive no weight in the quadrature estimation of the integral. This distribution is very flexible, being able to accurately represent most realistic fabric types. We provide details in Appendix A.

2.2. Fabric inference model

In this section we outline the inference procedure to estimate fabric eigenvalues from both sonic velocities and thin-section measurements while correcting for sampling error in the thin-section measurements, and smooth velocity drift in the sonic velocities.

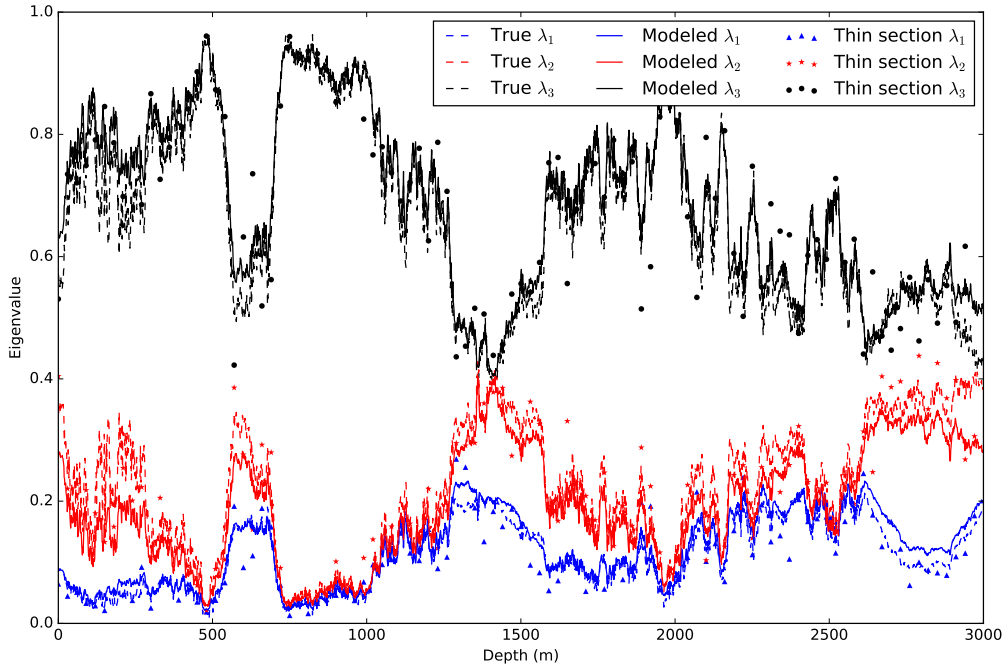


Fig. 1. Application of the statistical model to synthetically generated fabric. Thin-section eigenvalues with 30m spacing are generated by adding noise to the true eigenvalues. The modeled eigenvalues are close to the true eigenvalues over the majority of the depth. Error is primarily due to error in the velocity-correction term.

118 This procedure requires several steps, which can be summarized as follows: First, we use kriging (Cressie, 1993) to fit the
 119 observed eigenvalues of the thin-section data. Next, at each depth, we fit the discrete approximating distribution (Equation
 120 A1) to the smooth kriging estimates of the eigenvalues. Then, sonic velocities for the fitted discrete approximating distribution
 121 are found for each depth. This yields modeled sonic velocities from the thin-section data alone. If significant velocity drift or
 122 smooth model error are present, there will be large, low-frequency mismatches between the modeled velocity and observed
 123 velocities. This mismatch is distinct from the higher-frequency mismatch due to thin-section sampling error or small-scale
 124 fabric variability.

125 The smooth velocity mismatch is then regressed out using kriging to yield corrected velocities. Finally, the discrete ap-
 126 proximating distribution is fitted to the corrected velocities and the thin-section eigenvalues simultaneously. This then yields
 127 eigenvalue estimates incorporating information from both sonic velocity and thin-section data. We provide details in Appendix

128 B.

3. RESULTS

3.1. Eigenvalue inference on synthetic data

We now evaluate the statistical model developed in the previous section on synthetic fabric data. We generated “true” fabric eigenvalues for a 3000m deep borehole by assuming that the logit transformation of the eigenvalues are sampled from a Gaussian process with an exponential covariance function, to yield eigenvalues that are not smooth with depth. We then generate “true” v_p , v_{sh} , and v_{sv} velocities from these eigenvalues. We then add a smooth velocity corruption to these velocities (corresponding to model error and velocity drift), to yield synthetic corrupted velocities. The velocity corruption is the same value for v_{sh} , v_{sv} and v_p . However, we do not use this knowledge in fitting the model. Instead we fit a separate correction for each velocity. Synthetic thin-section samples were generated every 30m by adding noise averaging 0.2 to the logit-transformed eigenvalues at each depth, with 100 thin sections in total.

The results are plotted in Figure 1. Over the majority of the core, the true fabric eigenvalues are approximated accurately. In a few spots, larger errors occur due to mis-estimation of the velocity corruption. The estimated velocity corrections and the true velocity corruption are plotted in Figure 2. Typical errors are on the order of 10ms^{-1} .

Note that we do not add white noise to the synthetic velocity data, which would correspond to sonic velocity measurement error uncorrelated with depth. We expect that uncertainties in arrival times are the primary cause of non depth-correlated velocity errors. With velocities averaged over several runs, and smoothed over a few meters, this error would typically be small in comparison to the depth-correlated errors of model error and velocity drift.

3.2. Application to sonic measurements at NEEM

In this section, we apply the statistical model to P-wave velocity data and thin-section data collected at NEEM (Montagnat and others, 2014). Unlike the case with synthetic data, only P-wave velocities were collected. The P-wave velocity constrains only the concentration of c-axes in the vertical direction (associated with the largest fabric eigenvalue λ_3). However, due to the sum constraint of eigenvalues, this still provides information on the sum of λ_1 and λ_2 . The data were collected with a Mount Sopris CLP-4877 sonic-logging tool, modified to have a larger receiver spacing. The tool emits a monopole impulse source, which travels through the borehole fluid, through the ice, and back through the borehole fluid to two receivers, spaced at 90 cm and 303.5 cm from the source. Pulses are emitted every $2\text{ }\mu\text{s}$.

Three separate sonic logs were completed, with several sonic measurements taken every meter. Since the tool itself is roughly 3m long, spatial variability in sonic velocities shorter than 3 m are difficult to interpret. Thus, in our analysis, we take 3 m moving averages of the data. This also serves to significantly reduce uncorrelated measurement error, reducing error in measured v_p due to uncertainties in arrival times to the order of 1 ms^{-1} over multiple runs (Kluskiwicz and others, 2017).

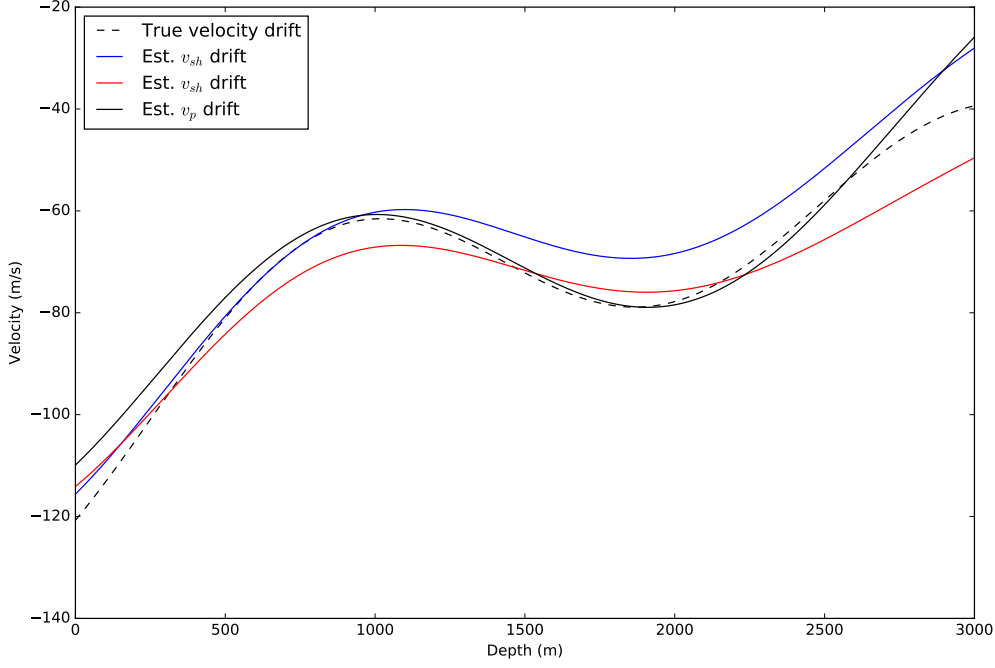


Fig. 2. Synthetic velocity corruption (dashed) and estimated velocity corrections (solid lines) for v_p , v_{sh} , and v_{sv} . Estimation of the velocity corruption depends on the thin-section eigenvalues. Due to the large degree of spatial variability of the fabric, and the noise in the thin sections, inaccuracies on the order of 10m/s occur. More thin-section samples, and more accurate samples, can reduce this error substantially.

158 The sonic velocity data were adjusted for pressure by $0.2 \text{ m s}^{-1} \text{ MPa}^{-1}$ (Helgerud and others, 2009), but were not adjusted
 159 for temperature due to the unavailability of borehole temperature measurements. However, borehole temperatures are typically
 160 very smooth with depth. Due to this, velocity errors due to temperature variations can be effectively corrected by our method
 161 in the absence of temperature measurements.

162 As discussed previously, large velocity drift occurs due to poor tool centralization in the borehole. This can differ between
 163 runs of the logging tool. However, short length-scale features are consistent between between runs.

164 We use the thin-section data from Montagnat and others (2014). There are 271 thin sections, taken from 34m to 2461m.
 165 At some depths, multiple thin sections are taken. This gives a rough indication of the sampling error of the thin sections at
 166 those depths. We apply the model only below 250m. Above this depth, the velocity model becomes increasingly inaccurate.
 167 We expect this is due to a higher concentrations of air bubbles in the ice.

168 In Figure 3, we plot the modeled P-wave velocities from NEEM thin sections, and the collected P-wave velocities. There
 169 is a significant mismatch, with the collected P-wave data typically being on the order of 100 m s^{-1} less than the modeled
 170 P-wave velocities. The lower-frequency part of this mismatch is due to some combination of model error and velocity drift.

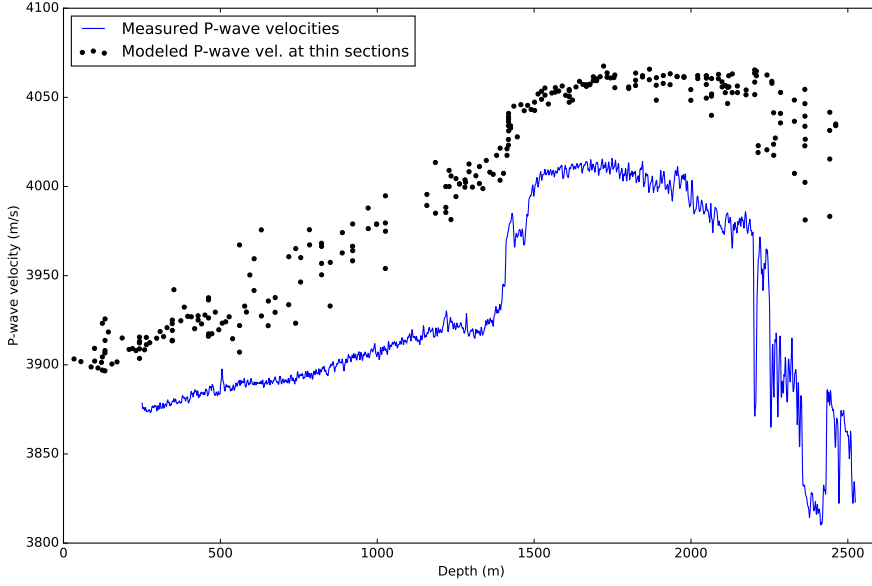


Fig. 3. P-wave velocities modeled from thin sections (dots) and observed P-wave velocities (line). The observed P-wave velocities are smoothed over 3m and are averaged over multiple runs. Due to a combination of model error and velocity drift, the observed velocities are on the order of 100m s^{-1} less than the modeled velocities.

We expect both to be smooth, as the assumptions of the statistical model require. In addition to these smooth errors, the velocities derived from thin sections have significant uncertainties due to sampling error.

In Figure 4, we plot the eigenvalues derived from thin sections along with eigenvalues estimated using both thin-section data and the collected P-wave velocity. The largest eigenvalue λ_3 increases almost linearly in the first 1300m of the core. Below about 2000m, the modeled eigenvalues begin to display large, high-frequency spikes. This may be due to differing amounts of dynamic recrystallization between layers. Layers experiencing greater amounts of recrystallization tend to have weaker fabrics. These fabric contrasts may also help initiate flow disturbances near the bed.

4. DISCUSSION

The proposed fabric inference method can produce more accurate eigenvalue estimates than using sonic velocities or thin-section data alone. In the synthetic dataset, error in inferred fabric is primarily due to error in thin-section measurements, which results in mis-estimation of the velocity correction term (see Figure 2). In particular, this can be seen in Figure 1 between 2800m and 3000m. Here, several synthetic thin-section samples in a row possess values of λ_3 significantly below the true values.

This is a particularly challenging synthetic dataset, with a great deal of short length-scale variability in the fabric eigenvalues. With only 100 noisy thin-section measurements it can be difficult to separate the effects of the velocity corruption from actual

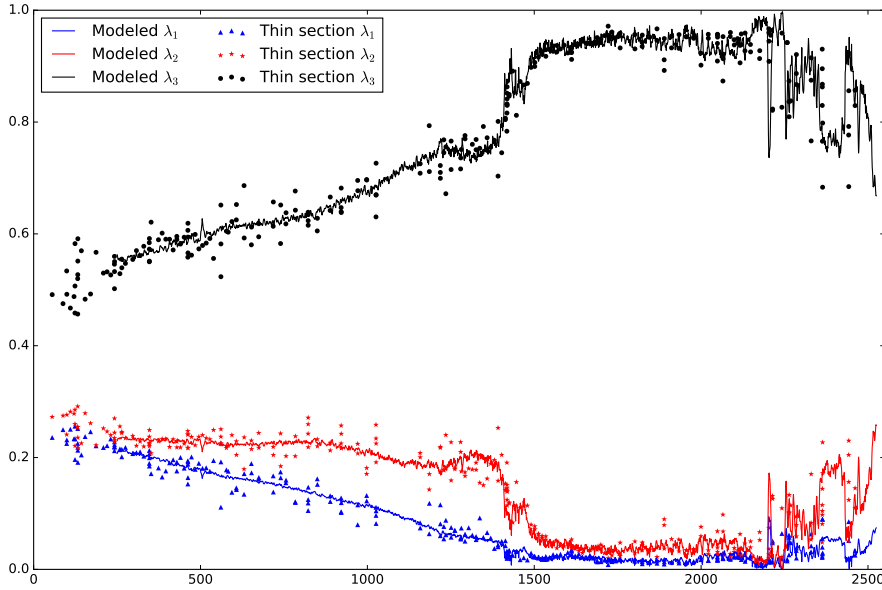


Fig. 4. Eigenvalues derived from thin sections at NEEM (dots) (Montagnat and others, 2014), together with spatially-continuous estimates from the assimilation procedure. The variability of eigenvalues over shorter length scales in the upper core appears to be due to sampling error. The large variations seen in the thin sections in the deep ice are confirmed by the sonic velocity data.

variability in fabric eigenvalues. Nonetheless, accuracy is still much better than relying solely on thin-section measurements. Thin-section eigenvalues can be expected to vary on short length-scales, therefore the error of one thin-section measurement cannot necessarily be improved by incorporating information from other, nearby, thin sections. This can be seen in Figure 1. The true fabric eigenvalues (dotted lines) vary over short length-scales with depth: it is not possible to separate this mode of variability from uncorrelated white noise in the synthetic thin-section eigenvalues (dots) using the thin-section data alone.

In contrast, the velocity mismatch, or drift (Equation B7), is smooth with depth. Thus, velocity mismatch estimates at one depth are correlated with those at nearby depths, significantly reduces the effects of white noise. This can be seen in from the variance of the velocity mismatch at a depth d' , $\epsilon_i(d')$ (Equation B10). Correlations between ϵ_i at depth d' and thin-section depths \mathbf{d}^{ts} , given by the vector $\mathbf{K}_{\epsilon_i}(d', \mathbf{d}^{ts})$, serve to reduce the variance of the estimated velocity mismatch. Applied to the NEEM ice-core data, we believe this model produces very accurate predictions of the largest eigenvalue, λ_3 . Other eigenvalues are not informed by the P-wave velocity, except due to the eigenvalue sum constraint. While the P-wave data provide information on the sum of λ_1 and λ_2 , it does not inform the difference between the two.

There are more thin sections, and much less large spatial variability in the NEEM core compared to the test on synthetic fabric. Thus, we expect the estimation of the velocity-correction term in the model to be more accurate, resulting in more accurate predictions of the largest eigenvalue λ_3 compared to the results for the synthetic data. Error in thin sections in

estimating the eigenvalues of the bulk fabric (in volumes sampled by the sonic tool) is on the order of 0.1 over most of the core, increasing in the recrystallized deep layers. These errors correspond to larger uncertainties in ice viscosity, due to the power-law rheology of ice.

We do not attempt to provide uncertainty information for the inferred fabric eigenvalues for this model, since tractable expressions for eigenvalue uncertainty in this model do not exist. Techniques such Markov chain Monte Carlo (Gilks, 2005) or variational Bayesian methods (Attias, 1999) may be useful for this purpose, but are outside the scope of this paper.

5. CONCLUSIONS

We showed P-wave velocity data collected from the NEEM ice core with a borehole sonic-logging tool. The collected P-wave velocities provide a high-quality continuous record of fabric over depth at scales longer than 3m. However, they are subject to smoothly-varying errors.

We derived a method of incorporating thin-section data and sonic-velocity data in order to gain a more accurate, and spatially continuous picture of the ODF. This is especially important for understanding stratigraphic disruption that occurs near the bed of NEEM and other cores. The inferred fabric from the NEEM core shows variability in fabric on the order of several meters. This may trigger or enhance stratigraphic disruption. Fabric variability on these length scales is impossible to observe with thin sections taken only every several meters, with large sampling error.

This work demonstrates the utility of combining different methods of ODF measurements. Future work measuring S-wave velocities will greatly enhance the capabilities of sonic-velocity measurements in ODF determination. Improved sonic tools could reduce velocity measurement error and bias. However, we still expect that thin-section measurements are a useful adjunct to provide a mostly unbiased ground-truth for ice-sheet fabric to correct velocity-model error.

REFERENCES

- Abadi, M., A. Agarwal, P. Barham, E. Brevdo, Z. Chen, G.S. Citro, C. Corrado, A. Davis, J. Dean, M. Devin and others, 2016. Tensorflow: Large-scale machine learning on heterogeneous distributed systems, *arXiv preprint arXiv:1603.04467*.
- Aki, K. and P.G. R., 1980. Quantitative Seismology: Theory and Methods.
- Alley, R.B., 1988. Fabrics in polar ice sheets: development and prediction, *Science*, **240**(4851), 493.
- Attias, H., 1999. Inferring parameters and structure of latent variable models by variational Bayes, Proceedings of the Fifteenth conference on Uncertainty in artificial intelligence, Morgan Kaufmann Publishers Inc., 21–30.
- Bentley, C.R., 1972. Seismic-wave velocities in anisotropic ice: A comparison of measured and calculated values in and around the deep drill hole at Byrd Station, Antarctica, *Journal of Geophysical Research*, **77**(23), 4406–4420.

- Bishop, C.M., 2006. Pattern recognition and machine learning, springer.
- Cressie, N., 1993. Statistics for spatial data: Wiley series in probability and statistics, *Wiley-Interscience New York*, **15**, 16.
- Duchi, J., E. Hazan and Y. Singer, 2011. Adaptive subgradient methods for online learning and stochastic optimization, *Journal of Machine Learning Research*, **12**(Jul), 2121–2159.
- Durand, G., A. Svensson, A. Persson, O. Gagliardini, F. Gillet-Chaulet, J. Sjolte, M. Montagnat and D. Dahl-Jensen, 2009. Evolution of the texture along the EPICA Dome C ice core, *Low Temperature Science*, **68**(Supplement), 91–105.
- Gagliardini, O., G. Durand and Y. Wang, 2004. Grain area as a statistical weight for polycrystal constituents, *Journal of Glaciology*, **50**(168), 87–95.
- Gilks, Walter R, 2005. Markov chain monte carlo, *Encyclopedia of Biostatistics*.
- Gusmeroli, A., E.C. Pettit, J.H. Kennedy and C. Ritz, 2012. The crystal fabric of ice from full-waveform borehole sonic logging, *Journal of Geophysical Research: Earth Surface*, **117**(F3).
- Helgerud, M.B., W.F. Waite, S.H. Kirby and A. Nur, 2009. Elastic wave speeds and moduli in polycrystalline ice Ih, sI methane hydrate, and sII methane-ethane hydrate, *Journal of Geophysical Research: Solid Earth*, **114**(B2).
- Hill, R., 1952. The elastic behaviour of a crystalline aggregate, *Proceedings of the Physical Society. Section A*, **65**(5), 349.
- Kennedy, J.H., E.C. Pettit and C.L. Di Prinzio, 2013. The evolution of crystal fabric in ice sheets and its link to climate history, *Journal of Glaciology*, **59**(214), 357–373.
- Kluskiwicz, D., E.D. Waddington, S. Anandakrishnan, D.E. Voigt, K. Matsuoka and M.P. McCarthy, 2017. Sonic Methods for Measuring Crystal Orientation Fabric in Ice, and results from the West Antarctica Ice Sheet Divide.
- Maurel, A., F. Lund and M. Montagnat, 2015. Propagation of elastic waves through textured polycrystals: application to ice, *Proc. R. Soc. A, The Royal Society*, vol. 471, 20140988.
- Maurel, A., J. Mercier and M. Montagnat, 2016. Critical investigation of calculation methods for the elastic velocities in anisotropic ice polycrystals, *The Cryosphere*, **10**, 3063–3070.
- Montagnat, M., N. Azuma, D. Dahl-Jensen, J. Eichler, S. Fujita, F. Gillet-Chaulet, S. Kipfstuhl, D. Samyn, A. Svensson and I. Weikusat, 2014. Fabric along the NEEM ice core, Greenland, and its comparison with GRIP and NGRIP ice cores.
- Placidi, L., R. Greve, H. Seddik and S.H. Faria, 2010. Continuum-mechanical, Anisotropic Flow model for polar ice masses, based on an anisotropic Flow Enhancement factor, *Continuum Mechanics and Thermodynamics*, **22**(3), 221–237.
- Sloan, I.H. and R.S. Womersley, 2004. Extremal systems of points and numerical integration on the sphere, *Advances in Computational Mathematics*, **21**(1-2), 107–125.
- Smith, E.C., A.F. Baird, J.M. Kendall, C. Martín, R.S. White, A.M. Brisbourne and A.M. Smith, 2017. Ice fabric in an Antarctic ice stream interpreted from seismic anisotropy, *Geophysical Research Letters*.

- 259 Thorsteinsson, T. and E.D. Waddington, 2002. Folding in strongly anisotropic layers near ice-sheet centers, *Annals of Glaciol-*
 260 *ogy*, **35**(1), 480–486.
- 261 Vogt, C., K. Laihem and C. Wiebusch, 2008. Speed of sound in bubble-free ice, *The Journal of the Acoustical Society of*
 262 *America*, **124**(6), 3613–3618.

263 APPENDIX A. NUMERICAL VELOCITY MODEL

We assume the support of discrete approximating distribution is confined to 900 “minimum energy” points \mathbf{c}_i^{mep} (Sloan and Womersley, 2004), which are approximately uniformly distributed over the sphere. Since the ODF is antipodally symmetric, we consider only the points on the upper hemisphere. The distribution is parameterized by unconstrained weights for each point, w_i . In order for the distribution to add up to unity, the probability measure at each point is given by,

$$\psi(\mathbf{c}_i^{mep}|\mathbf{w}) = \frac{\exp(w_i)}{\sum_j \exp(w_j)}, \quad (\text{A1})$$

264 where \mathbf{w} is the vector formed by weights w_i . This is known as softmax normalization (e.g. Bishop 2006). This distribution,
 265 which in this paper we will refer to as the discrete approximating distribution, has many more parameters than a typical
 266 PODF. However, over-fitting can be avoided by introducing a quadratic regularization penalty on the magnitude of the weight
 267 vector $\|\mathbf{w}\|$, similar to Tikhonov regularization.

268 To find the bulk stiffness, we rotate the stiffness tensor (Equation 2) such that the vertical axis of the transformed coordinate
 269 system is aligned with the c-axis of the quadrature point point \mathbf{c}_i^{mep} . This rotation is non-unique, since we assume that stiffness
 270 is invariant under rotations about the c-axis (in other words, we are not attempting to measure a-axes). We choose to rotate
 271 about the unique axis orthogonal to both \mathbf{c}_i^{mep} and the vertical direction in the global reference frame. Then, the bulk stiffness
 272 tensor is constructed by taking the sum of the stiffness tensors for each point \mathbf{c}_i^{mep} , weighted by the discrete approximating
 273 distribution (Equation A1). The squared velocities can then be found from the eigenvalues of the derived Christoffel matrix
 274 (Equation 4).

275 APPENDIX B. DETAILS OF THE FABRIC INFERENCE MODEL

276 In this section, we provide the mathematical details of this inference model. To start with, we will use Gaussian-process
 277 regression (Cressie, 1993), or kriging, to fit the observed thin-section data. A Gaussian process is a random function f whose
 278 values $\mathbf{y}_i = f(\mathbf{x}_i)$ at any finite number of points \mathbf{x}_i follow a multivariate normal distribution. The covariance matrix between
 279 sets of points \mathbf{X} and \mathbf{X}^* is $\mathbf{K}(\mathbf{X}, \mathbf{X}^*)$, where \mathbf{K} is a positive-definite covariance function, or kernel, giving the covariance
 280 between two points as a function of their location. This induces a spatial structure in the Gaussian process. For example,

a squared-exponential (or, Gaussian) kernel is often used. Here, \mathbf{K} is set to, $\mathbf{K}(\mathbf{X}, \mathbf{X}^*) = k \exp(-b\|\mathbf{X} - \mathbf{X}^*\|^2)$, where b is a constant giving the bandwidth of the Gaussian, and k is a scaling parameter. This favors smooth functions, because the correlation of nearby points is unity to first order. Gaussian white noise is also a Gaussian process, whose covariance function is $\mathbf{K}(\mathbf{x}, \mathbf{x}^*) = a$ if $\mathbf{x} = \mathbf{x}^*$, and zero otherwise. This indicates that the values at different points are uncorrelated but the value at a given point follows a univariate normal distribution.

Rather than working with eigenvalues directly, we instead fit the logit-transformed eigenvalues, η_i :

$$\boldsymbol{\eta} = \text{logit}(\boldsymbol{\lambda}) = \log(\boldsymbol{\lambda}) - \log(\lambda_3), \quad (\text{B2})$$

where $\boldsymbol{\lambda} = [\lambda_1, \lambda_2, \lambda_3]$, and $\boldsymbol{\eta} = [\eta_1, \eta_2, \eta_3]$. While the fabric eigenvalues are constrained to sum to unity, the logit eigenvalues η_i can take on any value. This makes the logits much easier to work with because the sum constraint is removed. The corresponding inverse softmax transformation squashes the logits back such that they sum to unity:

$$\lambda_i = \text{softmax}(\eta_i) = \frac{\exp(\eta_i)}{\sum_j \exp(\eta_j)}. \quad (\text{B3})$$

Let $\boldsymbol{\eta}^{ts}$ be the $N^{ts} \times 3$ matrix formed by the observed thin-section logit-transformed eigenvalues at each of the N^{ts} depths \mathbf{d}^{ts} of thin-section samples. We assume that each sample of logit-transformed eigenvalues are drawn from a realization of a Gaussian process, whose prior covariance is given by the sum of an exponential covariance function, $\exp(-a\|d' - d''\|)$ (where d' and d'' are arbitrary depths), and a white noise covariance function. The exponential covariance function allows for nonsmooth functions, because the nearby points are not perfectly correlated to first order (unlike the case with the squared-exponential covariance function). This is a more realistic covariance function than the squared-exponential covariance function, since observed fabric eigenvalues do seem to change abruptly with depth.

The predictive mean of the logit eigenvalues at a depth d' , conditioned on the observed thin-section logit eigenvalues $\boldsymbol{\eta}^{ts}$ at depths \mathbf{d}^{ts} , is given by,

$$\bar{\eta}_i(d') = \mathbf{K}(d', \mathbf{d}^{ts}) \mathbf{K}^{-1}(\mathbf{d}^{ts}, \mathbf{d}^{ts}) \boldsymbol{\eta}_i^{ts}, \quad (\text{B4})$$

where $\boldsymbol{\eta}_i^{ts}$ is the vector of the i^{th} logit-transformed eigenvalue η_i at each thin-section depth. The predictive variance of the the estimated logit eigenvalue η_i at depth d' is,

$$\text{Var}(\eta_i(d')) = \mathbf{K}(d') - \mathbf{K}(d', \mathbf{d}^{ts}) \mathbf{K}^{-1}(\mathbf{d}^{ts}, \mathbf{d}^{ts}) \mathbf{K}(\mathbf{d}^{ts}, d') \quad (\text{B5})$$

This mean and variance defines a normal distribution for the logit eigenvalues η_i at each depth. From this, at each depth d' we can fit the discrete approximating distribution (Equation A1) to these eigenvalues. This is done by minimizing the squared error between the predicted mean of η_i at depth d' , given by Equation (B4), and the calculated fabric eigenvalues from the

discrete approximating distribution (Equation A1). This is given by the eigenvalues of the estimated second-order orientation tensor $\hat{\mathbf{A}}$ of the discrete approximating distribution (Equation A1):

$$\hat{\mathbf{A}} = \sum_{\mathbf{c} \in \mathcal{M}} \mathbf{c} \mathbf{c}^T \psi(\mathbf{c} | \mathbf{w}), \quad (\text{B6})$$

293 where M is the set of minimum-energy points. If we assume that the fabric has a principal direction oriented nearly vertical,
294 then the estimated eigenvalues λ_i are given by the diagonal elements \hat{A}_{ii} (no sum) to first order.

At this point, for each depth we have fitted the discrete approximating distribution to the observed thin-section data, but not the observed velocities. We then calculate modeled sonic velocities for the fitted discrete approximating distribution at each depth. The calculated sonic velocities do not suffer from the drift of the observed sonic velocities, and are approximately correct on longer length scales, unlike the observed sonic velocities. However, due to the usually low spatial coverage of thin sections, the calculated sonic velocities do not detect the meter-scale features of fabric that the sonic-velocity measurements can (since the velocity measurements are taken nearly continuously with depth). We approximately correct this mismatch by using Gaussian-process regression to estimate the mismatch under the assumption that it is smooth. This will not remove the non-smooth, higher-frequency components of the velocity mismatch, which can instead be expected to correspond to actual short length-scale fabric variability, which is not captured by thin-section measurements. For each velocity v_i (either v_{sh} , v_{sv} , or v_p) the mismatch at a depth d' is,

$$\epsilon_i(d') = v_i^{ts}(d') - v_i^{obs}(d'), \quad (\text{B7})$$

where $v_i^{obs}(d')$ is the observed velocity at depth d' , and $v_i^{ts}(d')$ is the modeled velocity from the thin-section data. Here, we take the covariance function to be a sum of a squared-exponential covariance function, and white noise. This is given by,

$$\mathbf{K}_{\epsilon_i}(d, d') = k^{\epsilon_i} \exp(-a^{\epsilon_i} \|d - d'\|^2) + \sigma_{\epsilon_i}^2 I(d - d'), \quad (\text{B8})$$

where k^{ϵ_i} and $\sigma_{\epsilon_i}^2$ are scaling parameters, and a^{ϵ_i} is the bandwidth. I is a function where $I(0) = 1$, and $I(z) = 0$ for $z \neq 0$. This covariance produces smooth predictions, encoding a belief that the velocity drift is smooth. Similar to the Gaussian-process regression of the logit-transformed eigenvalues, the predicted mean of the the velocity mismatch is,

$$\bar{\epsilon}_i(d') = \mathbf{K}_{\epsilon_i}(d', \mathbf{d}^{ts}) \mathbf{K}_{\epsilon_i}^{-1}(\mathbf{d}^{ts}, \mathbf{d}^{ts}) \epsilon_i^{ts}. \quad (\text{B9})$$

The predictive variance is,

$$\text{Var}(\epsilon_i(d')) = \mathbf{K}_{\epsilon_i}(d') - \mathbf{K}_{\epsilon_i}(d', \mathbf{d}^{ts}) \mathbf{K}_{\epsilon_i}^{-1}(\mathbf{d}^{ts}, \mathbf{d}^{ts}) \mathbf{K}_{\epsilon_i}(\mathbf{d}^{ts}, d') \quad (\text{B10})$$

The modeled velocity is found from Equation (4). This then gives us the corrected velocities, with mean $\bar{v}_i^{corr} = v_i^{obs} + \bar{\epsilon}_i^{vel}$. Finally, at each depth d' , we simultaneously fit the discrete approximating distribution to the corrected velocities (Equation

B9) and the inferred thin-section logit-transformed eigenvalues $\bar{\eta}_i(d')$ (Equation B4). This is done by minimizing the following quantity with respect to the weights \mathbf{w} of the discrete approximating distribution at each depth of interest,

$$\begin{aligned}
 J(\mathbf{w}) = & \sigma_{sh}^{-2}(\hat{v}_{sh}(\mathbf{w}) - v_{sh}^{corr})^2 + \sigma_{sv}^{-2}(\hat{v}_{sv}(\mathbf{w}) - v_{sv}^{corr})^2 + \\
 & \sigma_p^{-2}(\hat{v}_p(\mathbf{w}) - v_p^{corr})^2 + \sigma_{\eta_1}^{-2}(\hat{\eta}_1(\mathbf{w}) - \bar{\eta}_1)^2 + \\
 & \sigma_{\eta_2}^{-2}(\hat{\eta}_2(\mathbf{w}) - \bar{\eta}_2)^2 + \sigma_{\eta_3}^{-2}(\hat{\eta}_3(\mathbf{w}) - \bar{\eta}_3)^2 + \alpha \|\mathbf{w}\|^2.
 \end{aligned} \tag{B11}$$

Here, σ_{sh}^2 is the variance of the velocity estimation, given by the sum of the variance of the velocity-correction term and the variance of the sonic-velocity measurements. The quantities σ_{sv} and σ_p are defined similarly. The quantity $\sigma_{\eta_i}^2$ is the variance of the posterior Gaussian process estimation of the logit-transformed fabric eigenvalue $\hat{\eta}_i$, given by Eq. (B5). The last term $\alpha \|\mathbf{w}\|^2$ is a regularization term, equivalent to putting a zero-mean Gaussian prior on the weights \mathbf{w} . This regularization term serves only to ensure that a unique minimum exists for the objective function (B11), rather than representing any kind of prior knowledge. The term is small enough that any fabric eigenvalues can be fit almost exactly. We minimized J with respect to \mathbf{w} using Adagrad gradient descent (Duchi and others, 2011), with the gradients derived using the Google Tensorflow automatic differentiation package (Abadi and others, 2016).

Note that the objective function (B11) is optimized independently at each depth of interest. We do not assume any kind of prior knowledge of smoothness with depth for this objective function. Sonic data collected from sonic tools are best averaged over a length-scale similar to the distance between the two sonic receivers. This accounts for short length-scale spatial correlations. There is no reason to assume that a fabric over longer length-scales is significantly correlated, since fabrics do indeed vary significantly over short length-scales. Assuming smoothness over longer length-scales would not allow for such short length-scale variability.